

# Nonlinear Loss Engineering in Near-Zero-Index Bulk Materials

Wallace Jaffray, Matteo Clerici, Bram Heijnen, Alexandra Boltasseva, Vladimir M. Shalaev, and Marcello Ferrera\*

Transparent conducting oxides (TCOs) show unprecedented optical nonlinearities in the near infrared wavelength range, where the real part of their linear refractive index approaches zero. More specifically, the Kerr nonlinearities of these materials have sparked widespread attention due to their magnitude and speed. However, due to the absorptive nature of these nonlinear processes, it is of fundamental interest to further investigate the imaginary component of the nonlinear index. The present work studies the nonlinear optical absorption properties of aluminium-doped zinc oxide (AZO) thin films in their near-zero-index (NZI) spectral window. It is found that the imaginary part of the refractive index is reduced under optical excitation such that the field penetration depth more than doubles. An optically induced shift of the NZI bandwidth of  $\approx 120$  nm for a pump intensity of  $1.3 \text{ TW cm}^{-2}$  is also demonstrated. Looking into the optically induced spectral redistribution of the probe signal, local net gain is recorded, which is ascribed to a nonlinear adiabatic energy transfer. The present study adds key information about the fundamental interplay between real and imaginary nonlinear indices in NZI media, while advancing parametric amplification as viable direction for loss compensation.

## 1. Introduction

Transparent conducting oxides (TCOs) have been widely used for industrial applications during the past two decades due to their transparency in the visible wavelength regime and conductivity. In the near-infrared spectral region, TCOs belong to the class of epsilon-near-zero (ENZ) materials where their real part of the dielectric permittivity vanishes, sprouting a series of fascinating optical phenomena<sup>[1,2,3]</sup> such as wavefront freezing,<sup>[3]</sup> enhanced superradiance,<sup>[4]</sup> super-coupling,<sup>[5]</sup> and light harvesting properties.<sup>[6]</sup> Furthermore, the scientific community has recently been intrigued by the optical properties of TCOs as near-zero-index (NZI) materials, which is a more stringent condition linked to enhanced optical nonlinearities.<sup>[7]</sup> The exact origin of this enhancement is still a point of contention within the photonics community, although different works point toward a slow light effect, linked directly to their

NZI nature.<sup>[8–12]</sup> Despite NZI and ENZ systems might display fundamentally different electrodynamic properties, sometimes these two definitions are used interchangeably.<sup>[13]</sup>


Initial key demonstrations of TCO's enhanced nonlinearities include optically induced unity-index shift,<sup>[14,15]</sup> and highly efficient frequency conversion.<sup>[16]</sup> More recent application-oriented efforts such as an NZI frequency resolved optical gating (FROG) system<sup>[17]</sup> and many NZI-enhanced modulator designs<sup>[18–20]</sup> have also shown great promise. However, so far, a great body of studies on TCOs' nonlinearities have been focused on Kerr effects for direct modulation of the optical phase. Here, we aim to shift the focus to the material losses and investigate how the complex refractive index changes under intense optical fluence. The nonlinear absorption of a material is inseparably tied to the phenomenon of saturable absorption (or reverse saturable absorption, depending on the sign). Saturable absorbers are materials or systems experiencing saturation in the maximum amount of absorbed light when exposed to sufficiently high optical intensities. Well known systems exhibiting saturable absorption include graphene<sup>[21]</sup>, carbon nanotubes<sup>[22,23]</sup>, semiconductors such as gallium arsenide, silicon, and indium gallium arsenide,<sup>[24]</sup> organic dyes<sup>[25]</sup>; transition metal dichalcogenides (layered materials with ultra-fast response times)<sup>[26]</sup>; quantum dots<sup>[27]</sup>; Kerr media<sup>[28,29]</sup>; and carbon black.<sup>[30]</sup> The most common applications exploiting saturable absorption typically relate to laser

W. Jaffray, B. Heijnen, M. Ferrera  
Institute of Photonics and Quantum Sciences  
Heriot-Watt University  
SUPA  
Edinburgh EH14 4AS, UK  
E-mail: m.ferrera@hw.ac.uk

M. Clerici  
James-Watt School of Engineering  
University of Glasgow  
Glasgow G12 8QQ, UK

B. Heijnen  
Department of Applied Physics and Eindhoven Hendrik Casimir Institute  
Eindhoven University of Technology  
Eindhoven 5600 MB, The Netherlands

A. Boltasseva, V. M. Shalaev  
Department of Physics & Astronomy and Birck Nanotechnology Center  
Purdue University  
West Lafayette, IN 47907, USA

 The ORCID identification number(s) for the author(s) of this article can be found under <https://doi.org/10.1002/adom.202301232>

© 2023 The Authors. Advanced Optical Materials published by Wiley-VCH GmbH. This is an open access article under the terms of the Creative Commons Attribution License, which permits use, distribution and reproduction in any medium, provided the original work is properly cited.

DOI: 10.1002/adom.202301232

mode-locking. Saturable absorption has also been previously investigated in the most widely used TCO, indium tin oxide (ITO). These studies have brought a few important facts to light. First, it is possible to modify TCO's saturable absorption properties by changing fabrication parameters such as substrate thickness,<sup>[31]</sup> or deposition temperature.<sup>[32]</sup> Second, saturable absorption can be reversed under high values of optical fluence.<sup>[31,32]</sup>

Our study focuses on the interplay between real and imaginary index and how this is instrumental for determining the efficiency of nonlinear processes, which are typically studied within the framework of Kerr nonlinearities. In this context, we investigated both internal and external efficiencies for a multilayer structure experiencing a strong optically induced change of its optical properties (i.e., complex permittivity). Besides reporting the transient absorption dynamics of TCO thin films, we also demonstrated how nonlinear spectral reshaping can mitigate losses near the ENZ wavelength region to achieve local gain. Our results underpin further development in the use of TCOs as ultrafast saturable absorbers and outlines a new direction for loss compensation in NZI bulk materials.<sup>[33,34]</sup>

## 2. Experimental Section

### 2.1. Materials

While many TCOs exhibit NZI properties with various wavelength dispersion curves, we focus our attention on aluminium-doped zinc oxide (AZO) as it exhibits a remarkably low linear attenuation coefficient in the near infrared window. Additionally, AZO does not contain rare earth metals, which are present in other widely studied TCOs<sup>[35]</sup> and is thus classified as a highly sustainable material. As for manufacturability, AZO can be deposited on a wide range of substrates via various CMOS-compatible methods and, most crucially, can be tuned to adjust the NZI window between 1200 and 2000 nm,<sup>[36]</sup> allowing us to tailor the material properties to fit a wide range of applications within and around the telecom bandwidths.

### 2.2. Experimental Methods

The study was carried out on a 900 nm thick film of AZO, which was deposited on a 0.5 mm thick fused silica substrate via pulsed laser deposition. As depicted in **Figure 1**, a pump-probe setup was utilized to investigate nonlinearities within the 1190 nm – 1550 nm range, while optical pumping occurs at 787 nm. The wavelength range of interest was set to center our investigation on the film's ENZ wavelength, which was located at 1310 nm. The pump was generated by a Ti:Sapphire laser producing a 100 Hz train of 90 fs pulses. Part of the pump was fed into an optical parametric amplifier (OPA), which generates the probe signal. The probe's intensity is negligible compared to the pump and does not "activate" nonlinearities on its own accord. Both the pump and probe were p-polarized and focused onto the AZO film, with a pump focal spot size of 250  $\mu\text{m}$  (full width at the  $1/e^2$  level). The delay between the pump and probe was varied, and the probe's absolute power in reflection and transmission was recorded at the maximum temporal overlap with the pump. This procedure

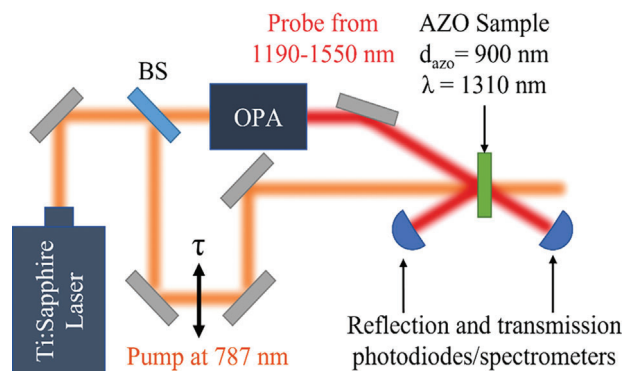


**Figure 1.** Pump and probe setup. A pump beam at 787 nm is scanned in time over a probe beam to activate AZO's NZI nonlinearities. The probe beam, tunable between 1190 nm and 1550 nm, is measured (with both photodiodes and a spectrometer) in both reflection and transmission, simultaneously. The AZO film has an ENZ wavelength of 1310 nm and a thickness of 900 nm.

was then repeated for multiple probe wavelengths within the selected range. From this set-up, it is possible to recover the linear refractive index by blocking the pump. Reintroducing the pump and repeating reflectance and transmittance measurements allows us to ascertain the nonlinearly modified index at various wavelengths. From these curves, it is also possible to evaluate the dispersion of the complex Kerr coefficient  $n_2$ .<sup>[7]</sup> The transmitted and reflected probe spectra were also recorded for various pump-probe delays and pump intensities ranging from 435  $\text{GW cm}^{-2}$  to 1304  $\text{GW cm}^{-2}$ . No film damage was observed for pump powers up to 2  $\text{TW cm}^{-2}$ .

### 2.3. Index Recovery

The linear complex index was evaluated starting from unpumped reflectance and transmittance measurements. Using acquired data, combined with prior knowledge of the material properties and appropriate models (see further discussions), it was possible to recover the real and imaginary refractive index via an alternative approach to ellipsometry, which was derived from the transfer matrix (TM) method.<sup>[37]</sup> From a practical point of view, while ellipsometry relies on the angular polarization analysis from a reflected broadband elliptical beam, our technique instead utilizes measurements of reflected and transmitted powers attained from a femtosecond probe at almost normal incidence. Such an approach is the most suitable in our case since it can be used in the presence of an optical pump, allowing for subsequent nonlinear analysis. It is worth noting that techniques such as Z-scan<sup>[38]</sup> can be used to recover  $n_2$ , and even higher order nonlinearities.<sup>[39]</sup> However, power series approximations can break down in the NZI enhancement regime,<sup>[40,41]</sup> an issue that the technique avoids by evaluating the direct nonlinear change in complex index. The well-known TM method is typically employed for finding reflectance and transmittance values from a known system with given complex refractive index. The problem takes the following mathematical form:

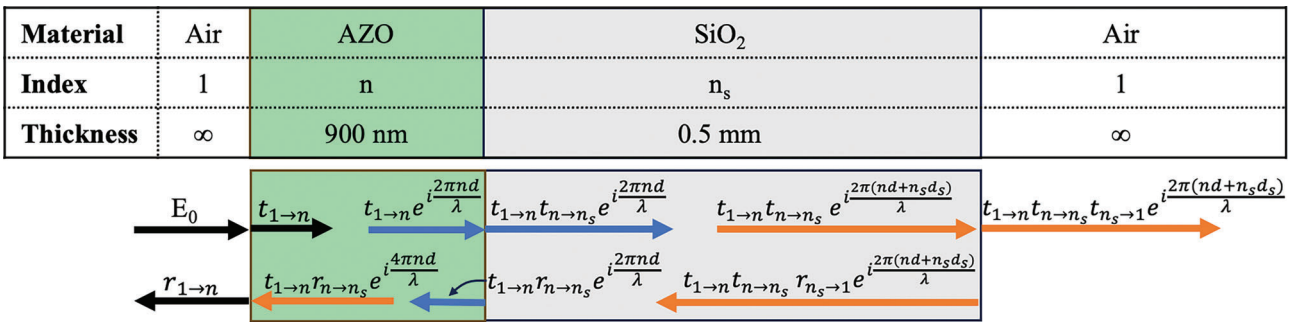


**Figure 2.** Schematic of transfer matrix method formulation. The table at the top of the figure provides the index and thickness for air, AZO, and SiO<sub>2</sub>. AZO has a thickness of 900 nm and index denoted by  $n$ , while the substrate SiO<sub>2</sub> is 0.5 mm thick and has an index denoted by  $n_s$ . Arrows denote transmission through our system at different stages. Equations above arrows show the coefficient associated with that stage of propagation. Black arrows have not propagated through any material, blue arrows have propagated through one layer, and orange arrows have propagated through any two layers.

$$\begin{bmatrix} 1 \\ r \end{bmatrix} = \mathbf{M} \begin{bmatrix} t \\ 0 \end{bmatrix} \quad (1)$$

$$\mathbf{M} = \frac{1}{t_{1 \rightarrow n} t_{n \rightarrow n_s} t_{n_s \rightarrow 1}} \begin{bmatrix} 1 & r_{n \rightarrow 1} \\ r_{1 \rightarrow n} & 1 \end{bmatrix} \begin{bmatrix} e^{i \frac{2\pi n d}{\lambda}} & 0 \\ 0 & e^{-i \frac{2\pi n d}{\lambda}} \end{bmatrix} \times \begin{bmatrix} 1 & r_{n_s \rightarrow n} \\ r_{n \rightarrow n_s} & 1 \end{bmatrix} \begin{bmatrix} e^{i \frac{2\pi n_s d_s}{\lambda}} & 0 \\ 0 & e^{-i \frac{2\pi n_s d_s}{\lambda}} \end{bmatrix} \begin{bmatrix} 1 & r_{1 \rightarrow n_s} \\ r_{n_s \rightarrow 1} & 1 \end{bmatrix} \quad (2)$$

Here  $n$  is the refractive index of the AZO film,  $d$  is its thickness,  $\lambda$  is the probe wavelength,  $n_s$  is the substrate index,  $d_s$  is the substrate thickness, and  $r$  and  $t$  are the complex reflection and transmission coefficients for the entire film system, respectively. The subscripts of the form  $n \rightarrow n_s$  denote the index of the materials that form the specified interface (where 1 is for air). The system represented by Equation 2 is explained into more details through **Figure 2**. Here, a table provides info about fundamental material parameters while the multi-block schematic below depicts the evolution of the field coefficients at every interface (up to two propagations in a layer). The index recovery path starts from the error functional  $Z(n)$  reported below:

$$Z(n) = \left| \left| \frac{M[1, 0]}{M[0, 0]} - R^{1/2} \right| + \left| \frac{1}{M[0, 0]} - T^{1/2} \right| \right| \quad (3)$$

Where the bracket notation indicates the matrix element such as  $M[\text{column}, \text{row}]$ ,  $R = |r|^2$ , and  $T = |t|^2$ . It is worth noting that the relation for  $T$  is more complex if the system does not start and finish with the same refractive index, in this case  $n = 1$  for input and output. The complex index  $n$  can be uniquely identified by finding the shared minimum between at least two  $Z(n)$  functionals with any combination of varying parameters (Incidence angle, polarization, substrate thickness, substrate index, etc.).

For experimental simplification, the angle of incidence was set at (almost) normal incidence ( $\ll 10$  deg) while the polarization was linear and arbitrarily set to p-polarization. Therefore, the direct minimization of the functional in Equation 3 would lead to multiple solutions at each wavelength. To identify a unique solution, while still performing one single measurement at a given wavelength, we select the closest one to our fitted Drude model for AZO<sup>[36]</sup> (See Supporting Information appendix A for Drude parameters fit). It is worth underlying that this final step

was equivalent to enforcing Kramers–Kronig conditions upon our physical system. In **Figure 3**, the results of this analysis are shown, where heatmaps are generated from  $1/|Z(n)|$  (rather than  $Z(n)$  for graphical clarity) for each measurement of  $R$  and  $T$  at different wavelengths. The dotted red line represents the fitted Drude model used to identify a single physical solution. The same process was used for the nonlinear analysis under optical pumping which is discussed along the subsequent paragraphs. The robustness of the methodology has also been tested by additional ellipsometer readings used to verify the linear case (See Supporting Information appendix B for ellipsometry comparison).

### 3. Results

#### 3.1. Material Analysis (Internal)

**Figure 4** displays real and imaginary refractive index of the studied AZO film from 1190 nm to 1550 nm (recovered via the method described in Section 2.3). The dashed blue lines refer to AZO's linear properties while the purple dotted line shows the index at which we consider the NZI condition to start ( $n_r < 0.2$ ).

The film shows extremely low real refractive index and rising absorption in the near infrared, as well as high transparency at lower wavelengths when the real index is approaching unity. Moving to the more relevant pumped case (yellow, green, and red dashed lines represent increasing pump intensities of 435 GW cm<sup>-2</sup>, 869 GW cm<sup>-2</sup>, and 1304 GW cm<sup>-2</sup>, respectively), it is evident that AZO's attenuation decreases as we increase pump power. As a point of reference, a pump intensity of 869 GW cm<sup>-2</sup> results in the field penetration depth, defined as  $\delta_e = \frac{\lambda}{2\pi \text{Im}(n)}$ , doubling with respect to the linear case (See Supporting Information appendix C). Contextually, the associated real index increases with the tendency to bring the material further from the NZI condition. Another important observation deals with the recorded nonlinear shift of the low index region toward longer wavelengths as the optical pumping is increased. We can also understand the magnitude of this shift from the bottom left panel of **Figure 4** that shows the real permittivity ENZ crossover points. In addition to this, the imaginary permittivity tends to increase with the pump power. All the above described trends are highlighted by the grey arrows in all panels of **Figure 4**. Finally, it is worth

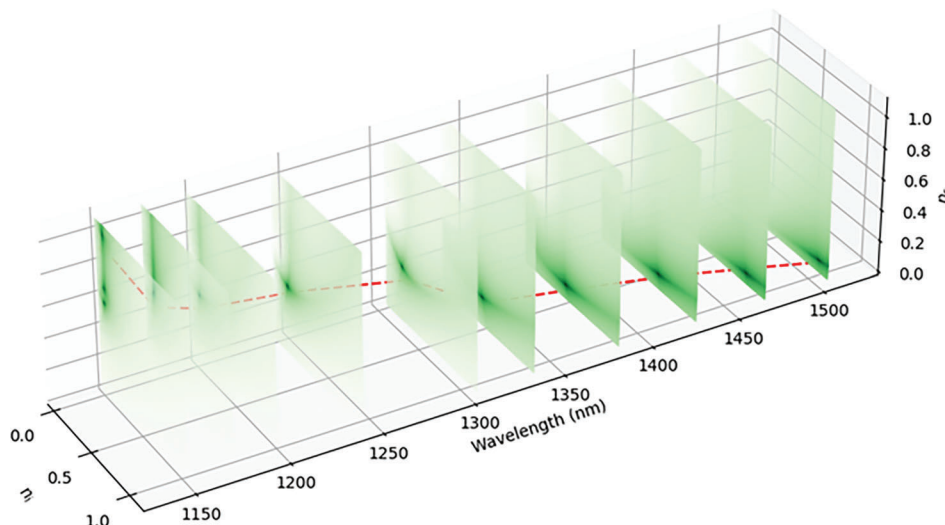


**Figure 3.** Evaluation of the linear complex index. Heatmaps placed at each wavelength plane show  $1/|Z(n)|$  for the measured values of  $R$  and  $T$  at each wavelength, where  $Z$  is the functional  $Z(n) = ||M[1,0]/M[0,0]|| - R^{1/2} + ||1/M[0,0]|| - T^{1/2}$  and  $M$  is the transfer matrix for our AZO-substrate system. Measurements were taken at almost normal incidence and p-polarization. Dotted red line shows fitted Drude model for AZO.

noting that nonlinear alteration of the material permittivity could be higher under degenerate pumping (i.e., same wavelength for both pump and probe photons) suggesting that an even more pronounced effect could be available when AZO is pumped in its NZI region (Up to a sixfold enhancement is estimated based on results reported.<sup>[42]</sup>)

### 3.2. Transient Internal Analysis

It is possible to calculate the transient imaginary index of the AZO film by measuring transmittance  $T(\lambda)$ , and reflectance  $R(\lambda)$  of the probe as a function of pump-to-probe time delay when knowing the input spectra  $I(\lambda)$ . Our analysis assumes that most

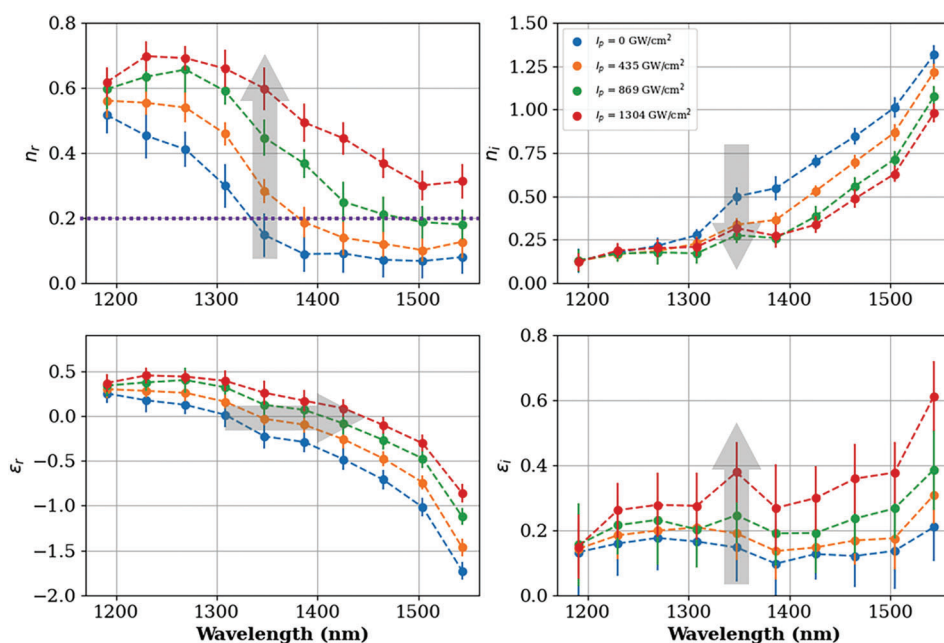


**Figure 4.** AZO's complex refractive index for various optical pump intensities. The index is retrieved via reflectance and transmittance measurements at various wavelengths and pump powers, while the pump and probe are overlapped temporally. The top panels display the real and imaginary components of index, while the bottom panels display the real and imaginary components of permittivity. Yellow, green, and red dashed lines represent pump intensities of  $435 \text{ GW cm}^{-2}$ ,  $869 \text{ GW cm}^{-2}$ , and  $1304 \text{ GW cm}^{-2}$ , respectively. As we increase the pump power, the real index increases, the ENZ crossover shifts toward higher wavelengths, the imaginary index drops considerably, thus reducing the film's absorption, and the imaginary permittivity increases. The grey arrows in all panels highlight these trends. Finally, the purple dotted line indicates where we consider the NZI condition to begin ( $n_r < 0.2$ ).

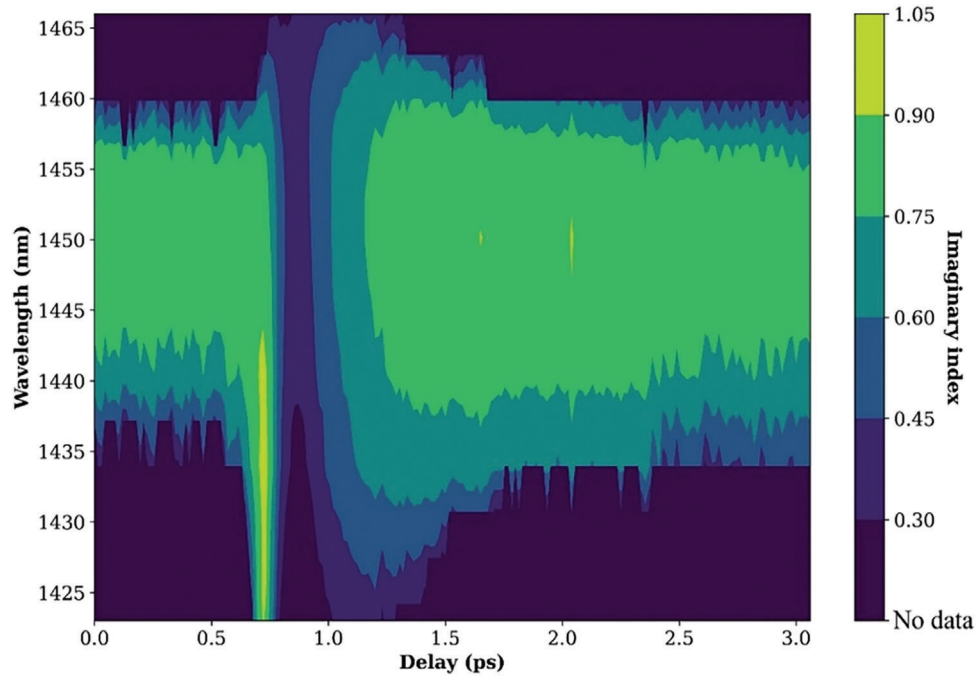


**Figure 5.** Transient imaginary index. Data are acquired for the probe at 1450 nm and the pump at 787 nm with an intensity of  $1087 \text{ GW cm}^{-2}$ . As expected, a clear relation between the linear index at low delays can be seen between this Figure and Figure 4. As the pump and probe overlap, the imaginary index drops substantially, thus increasing transparency near the probe's central wavelengths. This change in the imaginary index has a sharp rise time and a slower relaxation time on the order of 100s of femtoseconds as it is caused by a "slow", hot electron, nonlinearity.<sup>[8]</sup>

of the absorption occurs on the first pass transmission and subsequent reflection back through the film. This assumption is numerically sound due to AZO's relatively high absorption and the strong index contrast with the environment. With this in mind, we first estimate the frequency resolved transmittance of the probe's electric field through the initial air-AZO interface, which we label  $E_{start}(\lambda)$ . We then estimate the spectrum of the probe's electric field that reached the substrate, labeled  $E_{end}(\lambda)$ . From this, we can calculate the imaginary index of our sample as follows:

$$\text{Im}(n) = -\frac{\lambda}{2\pi d_{AZO}} \ln\left(\frac{E_{end}}{E_{start}}\right) \quad (4)$$

This method allows us to make a spectrally resolved analysis of the imaginary refractive index as the pump is swept in time over the probe. Results are shown in **Figure 5**, where a probe at 1450 nm is swept over by a pump at 787 nm with an intensity of  $1304 \text{ GW cm}^{-2}$ . The first and most valuable fact to notice is that the linear region at low values of delay (before the probe and pump are overlapped) has an imaginary index of  $\approx 0.8$ , which agrees with our previous analysis shown in Figure 4. As the pump and probe overlap, the film's imaginary index drops considerably to a value of  $\approx 0.3$ , which agrees with Figure 4, reducing the absorption of the AZO film at the maximum overlap. Further still, at shorter delays a region of higher loss can be seen for shorter wavelengths. We discounted the possibility that this feature is created via two-beam coupling as we are pumping in a non-degenerate configuration, which reduces the two beam coupling coefficients for  $n_2$  to the order of  $1 \times 10^{-4}$ .<sup>[43]</sup> This fea-

ture is instead magnified by an expected adiabatic frequency shift toward longer wavelengths, which effectively increases losses in this spectral window. Another factor we can notice is the speed of the material nonlinearity. As the pump overlaps the probe, the nonlinearity activates almost instantaneously, and the imaginary index drops very quickly within the pump pulse duration. The relaxation time for this nonlinearity is slower, on the order of 100s of femtoseconds.

### 3.3. Transient External Analysis

So far, we have only considered the internal material properties, however, from a more practical point of view it is important to look at the external efficiency of our multilayer system and evaluate what fraction of the incident light is absorbed. We anticipate that for this case a very different outcome is recorded with respect to the previously discussed observations. **Figure 6** displays a grid of heatmaps, each corresponding to a different central probe wavelengths (1150 nm, 1250 nm, and 1450 nm on the rows) and pump powers ( $435 \text{ GW cm}^{-2}$ ,  $652 \text{ GW cm}^{-2}$ ,  $869 \text{ GW cm}^{-2}$ , and  $1087 \text{ GW cm}^{-2}$  on the columns). The y-axis of these heatmaps is ranged over the measurable bandwidth of our probe pulse, the horizontal axis is the pump-probe delay, and the black line at 1310 nm identifies the ENZ wavelength. The metric measured in these heatmaps is the spectrally resolved overall loss of the film-substrate system,  $A(\lambda) = I(\lambda) - (R(\lambda) + T(\lambda))$ .

For simplicity, we first consider the linear points of Figure 6, which can be found at delay values for which pump and probe signals do not overlap. As the pump and probe are not

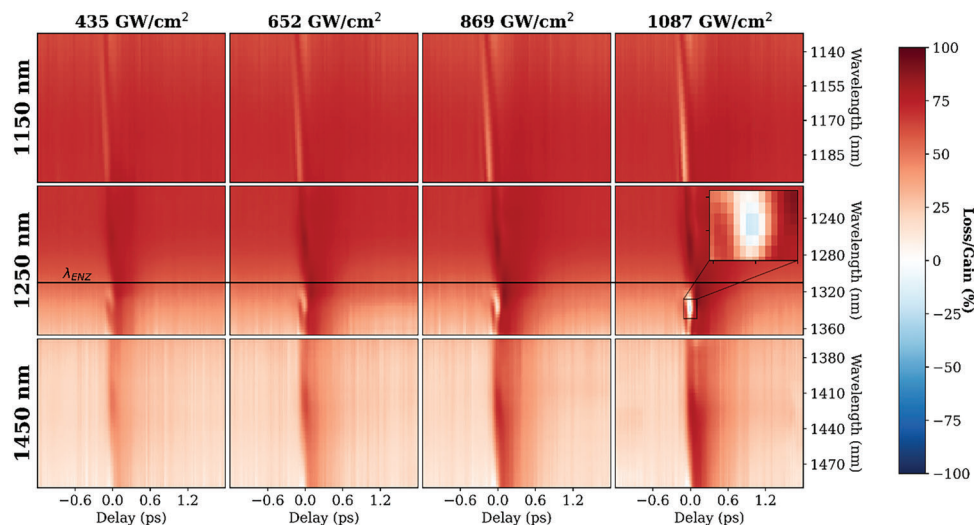


**Figure 6.** Loss/Gain heatmap for different probe central wavelengths and pump powers. Probe wavelengths include 1150 nm, 1250 nm, and 1450 nm, while pump intensities include  $435 \text{ GW cm}^{-2}$ ,  $652 \text{ GW cm}^{-2}$ ,  $869 \text{ GW cm}^{-2}$ , and  $1087 \text{ GW cm}^{-2}$  for a pump wave set at 787 nm. The black line marks the ENZ wavelength. Locally, net gain is achieved for a probe wavelength of 1250 nm and pump power of  $1087 \text{ GW cm}^{-2}$ . This is due to an adiabatic energy transfer that occurs because of the high nonlinearities and ultrafast response time of the material near the NZI point. The net gain area is highlighted by the magnified inset.

interacting at these delays, the specific column for the pump intensity becomes irrelevant.

An unmistakable gradient in the attenuation can be observed from 1150 nm to 1450 nm. The highest linear losses are at 1150 nm (relatively constant at  $\approx 75\%$ ), which then decrease near the ENZ wavelength at 1250 nm probe wavelength, leading to the lowest measured linear losses at 1450 nm. Comparing these results to those shown in Figure 4 leads to seemingly inconsistent results. Indeed, the imaginary index of the AZO film monotonically increases between 1190 nm and 1450 nm, which implies that losses should also increase. A simple explanation can be offered considering that the analysis shown in Figure 6 reports the total absorption as a fraction of the total input energy, whereas in Figure 4 the imaginary index is related to the internal absorption, that is the amount of energy absorbed by the material as a fraction of the in-coupled energy. Indeed, at 1150 nm, the reflectance from the film is about 1%, increasing to 27% at 1310 nm ( $\lambda_{\text{ENZ}}$ ) and, finally, reaching 80% at 1450 nm. Hence, although the material attenuation increases with wavelength, because the reflectance increases too, the overall effective losses are reduced.

Moving our consideration toward the nonlinear portion of Figure 6, we can discern three distinct regimes: i) optical pumping decreases attenuation; ii) optical pumping increases attenuation; iii) optical pumping creates local gain. Case (i) is most evident in the top row of Figure 6, for a probe wavelength of 1150 nm, where the measured attenuation is lowered from over 75% to below 25% at zero delay. Moving to case (ii), at a wavelength of 1450 nm (bottom row), we observe an opposite trend, and the losses increase at zero delay. Finally, for case (iii), nonlinear interaction leads to effective local gain. This gain occurs just above the ENZ wavelength and reaches a maximal value of  $\approx 20\%$ . An adiabatic energy transfer, consequent to a reshaping of the probe spectrum is responsible for the observed local gain, which we highlight in Figure 6 within the magnified inset.

## 4. Conclusions

In summary, we show that near-zero index nonlinearities can achieve large and ultra-fast optical modulation by exploiting absorptive processes. In this study, we examine the nonlinear optical absorption characteristics of aluminium-doped zinc oxide within its NZI window. We observe that under optical excitation the imaginary index decreases, leading to a more than doubled field penetration depth. Our study differentiates between internal and external performances where the former deals with the fundamental material characteristics and the latter pertains the input/output power of the entire multilayer structure. At the fundamental material level, optical pumping leads to a reduced optical absorption (i.e., reduced imaginary index) and a 118 nm shift of the low index region toward longer wavelengths. When instead we consider the external efficiency of our overall multilayer system, which accounts for input and output optical coupling, losses decrease as the wavelength increases. This is because the amount of light coupled at longer wavelengths (20% @ 1450 nm) is considerably lower than the value at shorter wavelengths (99% @ 1150 nm). In this regard, and for practical use, it is important to notice that around the crossover wavelength our photonic structure still operates with a 73% input efficiency. By analyzing both transmitted and reflected probe spectra under optical excitation, we identify three specific scenarios: i) reduced losses; ii) increased losses; iii) local amplification. As for the third case, the detected local gain is attributed to an adiabatic energy transfer facilitated by the material's giant nonlinearities. Furthermore, we demonstrate that the spectral redistribution of energy, resulting from the ultrafast alteration in the real part of the refractive index, can counterbalance losses in the vicinity of the ENZ wavelength region, leading to an effective local gain. These results provide important information for the design and fabrication of alternative ultra-fast modulation schemes employing TCOs, while also

providing alternative routes for loss compensation in NZI materials.

## Supporting Information

Supporting Information is available from the Wiley Online Library or from the author.

## Acknowledgements

The Heriot-Watt team wish to acknowledge economic support from the following: EPSRC project ID: EP/X035158/1 & AFOSR (EOARD) under Award No. FA8655-23-1-7254. M.C. acknowledges the support from UK Research and Innovation (UKRI), as the UK Engineering and Physical Sciences Research Council (EPSRC) (Fellowship "In-Tempo" EP/S001573/1), and Innovate UK, Application Number PN 10001572 (HiQuED). The Purdue co-authors acknowledge support by the U.S. Department of Energy, Office of Basic Energy Sciences, Division of Materials Sciences and Engineering under Award DE-SC0017717 (sample preparation) and the Air Force Office of Scientific Research (AFOSR) under Award No. FA9550-20-1-0124.

## Conflict of Interest

The authors declare no conflict of interest.

## Data Availability Statement

The data that support the findings of this study are available from the corresponding author upon reasonable request.

## Keywords

near-zero-index, nonlinear optics, epsilon-near-zero, integrated photonics, parametric amplification

Received: May 26, 2023

Revised: August 11, 2023

Published online:

- [1] N. Kinsey, C. DeVault, A. Boltasseva, V. M. Shalaev, *Nat. Rev. Mater.* **2019**, *4*, 742.
- [2] O. Reshef, I. De Leon, M. Z. Alam, R. W. Boyd, *Nat. Rev. Mater.* **2019**, *4*, 535.
- [3] I. Liberal, N. Engheta, *Nat. Photonics* **2017**, *11*, 149.
- [4] R. Fleury, A. Alu, *Phys. Rev. B* **2013**, *87*, 201101.
- [5] M. Silveirinha, N. Engheta, *Phys. Rev. Lett.* **2006**, *97*, 157403.
- [6] Y. Tian, F. P. Garcia de Arquer, C.-T. Dinh, G. Favraud, M. Bonifazi, J. Li, M. Liu, X. Zhang, X. Zheng, M. G. Kibria, S. Hoogland, D. Sinton, E. H. Sargent, A. Fratalocchi, *Adv. Mater.* **2017**, *29*, 1701165.
- [7] L. Caspani, R. P. Kaipurath, M. Clerici, M. Ferrera, T. Roger, J. Kim, N. Kinsey, M. Pietrzyk, A. Di Falco, V. M. Shalaev, A. Boltasseva, D. Faccio, *Phys. Rev. Lett.* **2016**, *116*, 233901.
- [8] J. B. Khurgin, M. Clerici, N. Kinsey, *Laser Photonics Rev.* **2021**, *15*, 2000291.
- [9] J. B. Khurgin, M. Clerici, V. Bruno, L. Caspani, C. DeVault, J. Kim, A. Shaltout, A. Boltasseva, V. M. Shalaev, M. Ferrera, D. Faccio, N. Kinsey, *Optica* **2020**, *7*, 226.
- [10] N. Kinsey, J. Khurgin, *Opt. Mater. Express* **2019**, *9*, 2793.
- [11] R. Secondo, A. Ball, B. Diroll, D. Fomra, K. Ding, V. Avrutin, U. Ozgur, D. O. Demchenko, J. B. Khurgin, N. Kinsey, *Appl. Phys. Lett.* **2022**, *120*, 031103.
- [12] M. Lobet, I. Liberal, L. Vertchenko, A. V. Lavrinenko, N. Engheta, E. Mazur, *Light: Sci. Appl.* **2022**, *11*, 110.
- [13] W. Jaffray, S. Saha, V. M. Shalaev, A. Boltasseva, M. Ferrera, *Adv. Opt. Photonics* **2022**, *14*, 148.
- [14] E. Feigenbaum, K. Diest, H. A. Atwater, *Nano Lett.* **2010**, *10*, 2111.
- [15] S. Benis, N. Munera, S. Faryadras, E. W. V. Stryland, D. J. Hagan, *Opt. Mater. Express* **2022**, *12*, 3856.
- [16] E. G. Carnemolla, W. Jaffray, M. Clerici, L. Caspani, D. Faccio, F. Biancalana, C. Devault, V. M. Shalaev, A. Boltasseva, M. Ferrera, *Opt. Lett.* **2021**, *46*, 5433.
- [17] W. Jaffray, F. Belli, E. G. Carnemolla, C. Dobas, M. Mackenzie, J. Travers, A. K. Kar, M. Clerici, C. DeVault, V. M. Shalaev, A. Boltasseva, M. Ferrera, *Nat. Commun.* **2022**, *13*, 3536.
- [18] H. W. Lee, G. Papadakis, S. P. Burgos, K. Chander, A. Kriesch, R. Pala, U. Peschel, H. A. Atwater, *Nano Lett.* **2014**, *14*, 6463.
- [19] E. Li, Q. Gao, R. T. Chen, A. X. Wang, *Nano Lett.* **2018**, *18*, 1075.
- [20] V. E. Babicheva, A. Boltasseva, A. V. Lavrinenko, *Nanophotonics* **2015**, *4*, 165.
- [21] X. Gan, R.-J. Shiue, Y. Gao, I. Meric, T. Heinz, K. Shepard, J. Hone, S. Assefa, D. Englund, *Nat. Photonics* **2013**, *7*, 883.
- [22] S. Set, H. Yaguchi, Y. Tanaka, M. Jablonski, *J. Lightwave Technol.* **2004**, *22*, 51.
- [23] Z. Sun, A. G. Rozhin, F. Wang, T. Hasan, D. Popa, W. O'Neill, A. C. Ferrari, *Appl. Phys. Lett.* **2009**, *95*, 253102.
- [24] A. Gluth, Y. Wang, V. Petrov, J. Paajaste, S. Suomalainen, A. Härkönen, M. Guina, G. Steinmeyer, X. Mateos, S. Veronesi, M. Tonelli, J. Li, Y. Pan, J. Guo, U. Griebner, *Opt. Express* **2015**, *23*, 1361.
- [25] A. Lennert, K. Wagner, R. Yunis, J. M. Pringle, D. M. Guldi, D. L. Officer, *ACS Appl. Mater. Interfaces* **2018**, *10*, 32271.
- [26] A. Grubišić Čabo, J. A. Miwa, S. S. Grønborg, J. M. Riley, J. C. Johannsen, C. Cacho, O. Alexander, R. T. Chapman, E. Springate, M. Grioni, J. V. Lauritsen, P. D. C. King, P. Hofmann, S. Ulstrup, *Nano Lett.* **2015**, *15*, 5883.
- [27] D. Auth, S. Liu, J. Norman, J. E. Bowers, S. Breuer, *Opt. Express* **2019**, *27*, 27256.
- [28] T. Brabec, C. Spielmann, P. F. Curley, F. Krausz, *Opt. Lett.* **1992**, *17*, 1292.
- [29] G. Agrawal, N. Olsson, *IEEE J. Quantum Electron.* **1989**, *25*, 2297.
- [30] D. Z. Mohammed, A. H. Al-Janabi, *Laser Physics* **2016**, *26*, 115108.
- [31] T. Yan, R. Hong, C. Tao, Q. Wang, H. Lin, Z. Han, D. Zhang, *Optical Materials* **2022**, *125*, 112061.
- [32] H. Ma, Y. Zhao, Y. Shao, Y. Lian, W. Zhang, G. Hu, Y. Leng, J. Shao, *Photonics Research* **2021**, *9*, 678.
- [33] C. Rizza, A. D. Falco, A. Ciattoni, *Appl. Phys. Lett.* **2011**, *99*, 221107.
- [34] A. Mischok, N. Hale, M. C. Gather, A. Di Falco, *J. Appl. Phys.* **2021**, *129*.
- [35] J. H. Gu, L. Long, Z. Lu, Z. Y. Zhong, *J. Mater. Sci.: Mater. Electron.* **2015**, *26*, 734.
- [36] G. V. Naik, V. M. Shalaev, A. Boltasseva, *Adv. Mater.* **2013**, *25*, 3264.
- [37] A. Lakhtakia, T. G. Mackay, *The transfer-matrix method in electromagnetics and Optics*, Morgan & Claypool Publishers, Kentfield CA **2020**.
- [38] M. Sheik-Bahae, A. A. Said, T. H. Wei, D. J. Hagan, E. W. Van Stryland, *Journal of Quantum Electronics* **1990**, *26*, 760.
- [39] G. Tsigaridas, M. Fakis, I. Polyzos, P. Persephonis, V. Giannetas, **2003**, *225*, 253.
- [40] M. Z. Alam, I. De Leon, R. W. Boyd, *Science* **2016**, *352*, 795.
- [41] O. Reshef, E. Giese, M. Z. Alam, I. De Leon, J. Upham, R. W. Boyd, *Opt. Lett.* **2017**, *42*, 3225.
- [42] E. G. Carnemolla, L. Caspani, C. DeVault, M. Clerici, S. Vezzoli, V. Bruno, V. M. Shalaev, D. Faccio, A. Boltasseva, M. Ferrera, *Opt. Mater. Express* **2018**, *8*, 3392.
- [43] J. Paul, M. Miscuglio, Y. Gui, V. J. Sorger, J. K. Wahlstrand, *Opt. Lett.* **2021**, *46*, 428.